IEEE Photonics Journal
An IEEE Photonics Society Publication

Open Access

High-Speed Compressive Microscopy of Flowing Cells Using Sinusoidal Illumination Patterns

Volume 9, Number 1, February 2017

Qiang Guo
Hongwei Chen, *Senior Member, IEEE*
Yuxi Wang
Yong Guo
Peng Liu
Xiurui Zhu
Zhen Cheng
Zhenming Yu
Sigang Yang
Minghua Chen
Shizhong Xie, *Senior Member, IEEE*

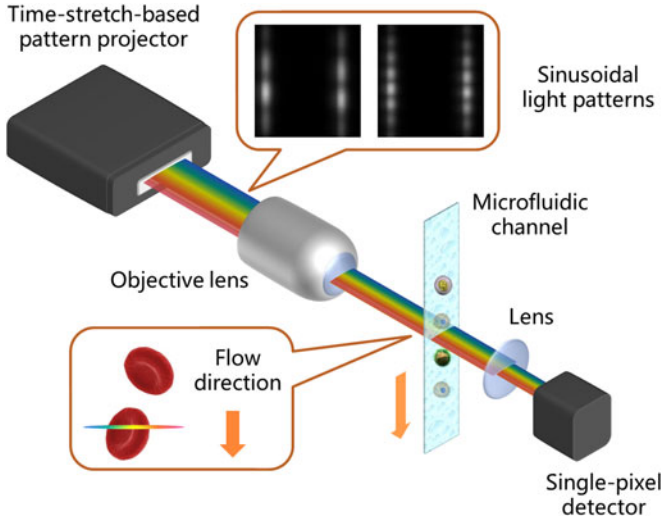

DOI: 10.1109/JPHOT.2016.2644869
1943-0655

IEEE photonics SOCIETY

IEEE

High-Speed Compressive Microscopy of Flowing Cells Using Sinusoidal Illumination Patterns

Qiang Guo,[1] Hongwei Chen,[1] *Senior Member, IEEE*, Yuxi Wang,[1] Yong Guo,[2] Peng Liu,[2] Xiurui Zhu,[2] Zhen Cheng,[2] Zhenming Yu,[1] Sigang Yang,[1] Minghua Chen,[1] and Shizhong Xie,[1] *Senior Member, IEEE*

[1]Department of Electronic Engineering, Tsinghua National Laboratory for Information Science and Technology,Tsinghua University, Beijing 100084, China
[2]Department of Biomedical Engineering, School of Medicine, Collaborative Innovation Center for Diagnosis and Treatment of Infectious Diseases, Tsinghua University, Beijing 100084, China

DOI:10.1109/JPHOT.2016.2644869

Manuscript received November 7, 2016; revised December 15, 2016; accepted December 20, 2016. Date of publication December 23, 2016; date of current version January 10, 2017. This work was supported in part by National Natural Science Foundation of China under Contract 61322113 and Contract 61271134; in part by the young top-notch talent program sponsored by the Ministry of Organization, China; and in part by the Tsinghua University Initiative Scientific Research Program. Corresponding author: H. Chen (e-mail: chenhw@mail.tsinghua.edu.cn).

Abstract: Single-pixel imaging (SPI) exploits the sparsity structure of natural images and enables image acquisition with far fewer measurements than the number of pixels. However, current SPI devices suffer from low imaging speed and an extremely time-consuming image reconstruction operation. Photonic time-stretch (PTS) technique is demonstrated to enable high-speed structured-illumination pattern generation, which significantly accelerates the imaging speed of conventional SPI devices. Meanwhile, to achieve fast image reconstruction, phase-shifted sinusoidal illumination patterns are used to acquire the Fourier spectrum of images and then a simple inverse fast Fourier transform (IFFT) operation is required for image reconstruction, which is quite computationally efficient. This paper presents a high-speed real-time compressive imaging system and its applications to imaging flow cytometry. Not only is a 625-kHz frame rate demonstrated, which is three orders of magnitude higher than that of a conventional SPI device, but the reconstruction process is remarkably accelerated as well, which enables our prototype system to operate in real time.

Index Terms: Single-pixel imaging, imaging flow cytometry, sinusoidal illumination patterns, Fourier spectrum acquisition.

1. Introduction

Computational imaging (CI) using projected patterns enables image acquisition with spatially unresolved detectors and covers a significantly broader spectral range than conventional charge-coupled device (CCD) or complementary metal-oxide semiconductor (CMOS) cameras [1]–[3]. Single-pixel imaging (SPI), which is based on the theory of compressed sensing (CS), exploits the sparsity structure of natural images and enables image acquisition with far fewer measurements than the total number of pixels [4]–[6]. Conventional SPI devices employ digital micromirror devices (DMDs) or spatial light modulators (SLMs) for illumination pattern generation. However, the pattern generation rate is largely constrained by the scanning speed of mechanical mirrors or the response

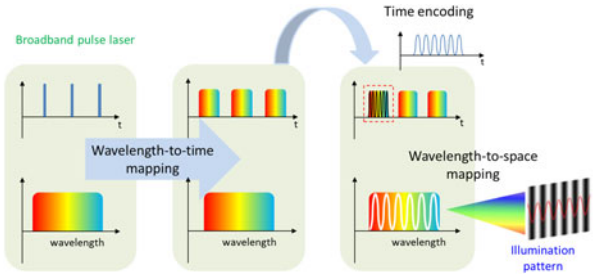

Fig. 1. Basic principle of the high-speed illumination pattern generation method.

time of DMD/ SLMs, both of which are typically on the order of milliseconds [6]–[13]. In order to overcome the speed limitation of conventional SPI devices, an approach to achieving rapid generation of projected patterns should be found. In recent years, ultrafast illumination pattern generation is demonstrated through spectral pulse shaping based on photonic time-stretch (PTS) and wavelength-to-space conversion [14]–[18]. Thus, the pattern generation rate is determined by the pulse repetition rate which is three orders of magnitude higher than the switching rate of the DMD. Using this illumination pattern generation method, the imaging speed of the single-pixel camera can reach hundreds of kHz or even several MHz [19]–[22]. Such a high-speed single-pixel camera can be used to observe fast dynamic phenomena, for example, high-throughput screening of flowing cells. The major advantage is its ability to compress the data produced by high-throughput instruments [16] (from several gigabytes per second to tens of megabytes per second), greatly relieving the burden of data acquisition, transmission and storage. However, according to the theory of CS, reconstructing an image (especially a high-resolution image) is relatively time-consuming, which presents a challenge to real-time signal processing.

In this paper, we exploit the fact that most of the information present in the image has been packed into a small number of Fourier coefficients (namely low spatial frequency components). The coefficients that provide little image information (high spatial frequency components) can be discarded, resulting in a slightly degraded version of the original image. Thus only an inverse fast Fourier transform (IFFT) operation is required for image reconstruction, which is quite computationally efficient. Based on this principle, we propose a novel high-speed SPI scheme that produces high-quality images by acquiring their Fourier spectrum. Phase-shifted sinusoidal illumination patterns are employed for spectrum acquisition [23] and an inverse fast Fourier transform (IFFT) operation is used to achieve real-time image reconstruction. We apply our system to flow cytometry and an imaging flow cytometer with a throughput of 30,000 cells/s is demonstrated. Compared with the previous SPI devices [14]–[22], our prototype system not only enables high-frame-rate microscopy with data compression capability, but also achieves real-time image reconstruction. In addition, compared with other image compression systems based on photonic time stretch (using a digitizer with a sampling rate of several GS/s) [24]–[26], our system only needs to acquire data at a rate of a few hundred MS/s, greatly relieving the burden of data acquisition, transmission, and storage. In this article, we will introduce the key principle of our scheme, present the system prototype and demonstrate real-time compressive microscopy of various flowing cells.

2. Principle

2.1. Principle of High-Speed Illumination Pattern Generation

The imaging speed of a conventional single-pixel camera is currently limited by the response time of the DMD. The key feature of our scheme is its ability to generate illumination patterns at high speed (approximately several tens of MHz). Fig. 1 illustrates the basic principle of this illumination pattern generation method. Here a femtosecond fiber laser with a high repetition rate is used as the light source (see the left side of Fig. 1). First, the spectrum of the emitted optical pulse is mapped to a temporal waveform by using a dispersive element, e.g., dispersion compensating fibers (DCFs) or chirped fiber Bragg gratings (CFBGs) (see the middle of Fig. 1). Then, the dispersed pulse is

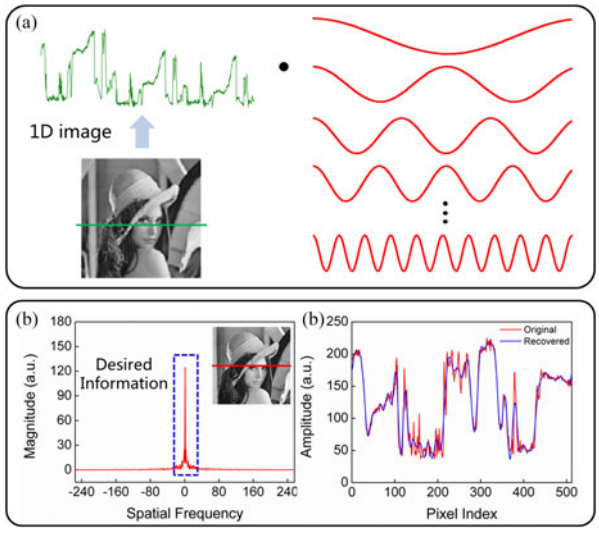

Fig. 2. Basic principle of Fourier spectrum acquisition. (a) Image acquisition (here, 1-D images) is achieved by means of Fourier spectrum acquisition using sinusoidal patterns. (b) Most of the information present in the image concentrates on low spatial frequency components. (c) Reconstructed 1-D images using low spatial frequency components (blue line) and all the spatial frequency components (red line).

spectrally shaped via modulation of light intensity, and a spatially dispersive medium is used to achieve wavelength-to-space conversion for providing the predetermined illumination patterns (see the right side of Fig. 1). Here, a diffraction grating is used to generate 1-D illumination patterns and a pair of orthogonally oriented spatial dispersers is used to generate 2-D patterns. Utilizing the method presented here, the pattern generation rate can reach tens of MHz, which is three orders of magnitude higher than that achieved by DMDs (22 kHz).

2.2. Principle of Fourier Spectrum Acquisition

Another key feature of our scheme is that it enables image acquisition (here, 1-D images) using sinusoidal patterns instead of binary patterns, as shown in Fig. 2(a). Thus the measurements captured by the single-pixel detector are the coefficients of different spatial frequencies in the image. Therefore only a simple IFFT operation is required to perform image reconstruction, which is much more computationally efficient than the reconstruction algorithms used in previous CS-based schemes. In addition, as most of the information present in the image concentrates on low spatial frequency components (see Fig. 2(b)), we can achieve image compression by discarding high spatial frequency components to obtain a slightly degraded version of the original image, as shown in Fig. 2(c). It is a common practice in image compression (e.g., Joint Photographic Experts Group), which can improve the imaging speed of our scheme. Next, the mathematical model will be introduced in detail.

Our scheme is based on the Fourier transformation, which can be expressed as:

$$\begin{bmatrix} X(0) \\ X(1) \\ X(2) \\ \vdots \\ X(N-1) \end{bmatrix} = \begin{bmatrix} 1 & 1 & 1 & \cdots & 1 \\ 1 & W_N^1 & W_N^2 & \cdots & W_N^{(N-1)} \\ 1 & W_N^2 & W_N^4 & \cdots & W_N^{2(N-1)} \\ \vdots & \vdots & \vdots & \ddots & \vdots \\ 1 & W_N^{N-1} & W_N^{2(N-1)} & \cdots & W_N^{(N-1)(N-1)} \end{bmatrix} \begin{bmatrix} x(0) \\ x(1) \\ x(2) \\ \vdots \\ x(N-1) \end{bmatrix}$$

$$W_N^K = e^{-j\frac{2\pi}{N}K} = \cos\left(\frac{2\pi}{N}K\right) - j\sin\left(\frac{2\pi}{N}K\right)(K = 0, 1, \cdots \mathrm{N}-1) \quad (1)$$

where $x(n)(n = 0, 1, \cdots N-1)$ denotes a signal, and $X(k)(k = 0, 1, \cdots N-1)$ is its Fourier transform. As can be seen in (1), the coefficient at each frequency is a complex number and its real part (or imaginary part) is the inner product between the signal and a cosinoidal signal (or a sinusoidal signal) at the corresponding frequency. Our scheme utilizes the aforementioned method to generate high-speed sinusoidal light patterns to illuminate a scene and then acquires the reflected light with a single-pixel detector. The captured measurements are the spectral coefficients of the illuminated scene and thus only a simple IFFT operation is required for image reconstruction.

To obtain the Fourier spectrum of the image, four-step phase-shifted sinusoidal illumination patterns need to be generated with the aforementioned method. The switching rate of the generated patterns is equal to the pulse repetition rate f_{rep} and their spatial frequencies are harmonics of the fundamental frequency f_0. Here we set $f_0 = f_{rep}$. For a certain spatial frequency $f_i = i \cdot f_0$, there are four patterns with different initial phases φ (0, $\pi/2$, π and $3\pi/2$). Assuming that the output after optical intensity modulation in the time domain is given by

$$P_{out}(t, f_i) = \frac{1}{2} P_{in}(t)[1 + \alpha \cos(2\pi f_i t + \varphi)] \tag{2}$$

where $P_{in}(t)$ denotes the input optical pulse train. $\alpha = \pi / V_\pi$ is the modulation index of the electro-optic intensity modulator, where V_π is the half-wave voltage. The time-to-wavelength conversion (also known as dispersive Fourier transformation) is mainly a linear mapping [15], and consequently the intensity of the dispersed pulse mimics its spectrum. Then, a diffraction grating is used to generate the corresponding 1D illumination patterns. As the wavelength-to-space mapping is also a linear process [15], the generated patterns can be written as

$$C_{out}(x, f_x) = A + B \cos(2\pi f_x x + \varphi) \tag{3}$$

where A and B account for the average brightness and the fringe contrast, respectively. f_x is the corresponding spatial frequency of the generated illumination patterns, where x denotes the spatial position along the length of the 1-D illumination patterns. The light reflected from the scene is collected by a bucket detector. The captured measurements are expressed as

$$V_\varphi(f_x) = K \int_x I(x) C_{out}(x, f_x) dx + V_n \tag{4}$$

where $I(x)$ is the intensity distribution of the illuminated scene. K is a constant and V_n is the noise term. Each complex Fourier coefficient can be obtained from four measurements (V_0, $V_{\pi/2}$, V_π, and $V_{3\pi/2}$) as follows:

$$[V_0(f_x) - V_\pi(f_x)] + j \cdot [V_{\pi/2}(f_x) - V_{3\pi/2}(f_x)] = K \omega_{f_x} \tag{5}$$

where ω_{f_x} is the Fourier coefficient at spatial frequency f_x. When M measurements are acquired (namely $\omega_0, \omega_{f_0}, \cdots, \omega_{Mf_0}$) and the values of the Fourier coefficients at high frequencies (namely $\omega_{(M+1)f_0}, \omega_{(M+2)f_0}, \cdots, \omega_{(N-1)f_0}$) are all set to zero, we can perform IFFT to reconstruct the original 1-D image $I(x)$ as follows:

$$\begin{bmatrix} I(0) \\ I(1) \\ \vdots \\ I(M) \\ I(M+1) \\ \vdots \\ I(N) \end{bmatrix} = \frac{1}{N} \begin{bmatrix} 1 & 1 & \cdots & 1 & 1 & \cdots & 1 \\ 1 & W_N^{-1} & \cdots & W_N^{-M} & W_N^{-(M+1)} & \cdots & W_N^{-(N-1)} \\ \vdots & \vdots & \ddots & \vdots & \vdots & \ddots & \vdots \\ 1 & W_N^{-M} & \cdots & W_N^{-M \cdot M} & W_N^{-M \cdot (M+1)} & \cdots & W_N^{-M \cdot (N-1)} \\ 1 & W_N^{-(M+1)} & \cdots & W_N^{-(M+1) \cdot M} & W_N^{-(M+1) \cdot (M+1)} & \cdots & W_N^{-(M+1) \cdot (N-1)} \\ \vdots & \vdots & \ddots & \vdots & \vdots & \ddots & \vdots \\ 1 & W_N^{-(N-1)} & \cdots & W_N^{-(N-1) \cdot M} & W_N^{-(N-1) \cdot (M+1)} & \cdots & W_N^{-(N-1)(N-1)} \end{bmatrix} \begin{bmatrix} \omega_0 \\ \omega_{f_0} \\ \vdots \\ \omega_{(M-1)f_0} \\ 0 \\ \vdots \\ 0 \end{bmatrix}. \tag{6}$$

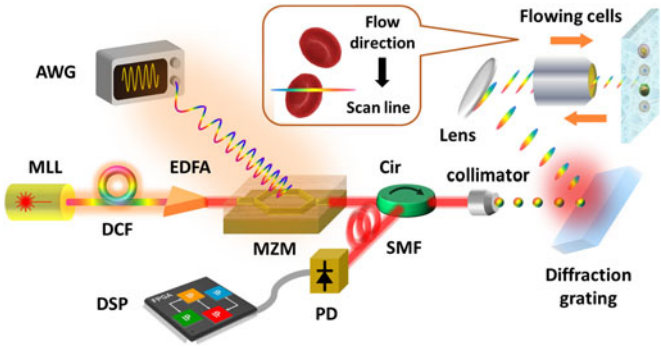

Fig. 3. Experimental setup. MLL, mode-locked laser; DCF, dispersion compensating fiber; EDFA, erbium-doped fiber amplifier; MZM, Mach-Zehnder modulator; AWG, arbitrary waveform generator; Cir, circulator; SMF, single mode fiber; PD, photo-detector; DSP, digital signal processor.

3. Experimental Setup

The schematic diagram of the proposed scheme is shown in Fig. 3. The light source is a mode-locked laser (MLL) emitting an optical pulse train with a repetition rate of 50 MHz, a center wavelength of 1550 nm and a pulse width of 150 fs. The optical pulses pass through a section of dispersion compensating fiber (DCF) with a group velocity dispersion (GVD) of -1368 ps/nm. Then each optical pulse is temporally stretched to about 20 ns. To compensate for the dispersion-induced power penalty, a high-power erbium-doped fiber amplifier (EDFA) (Amonics AEDFA-33-B-FA) is used to amplify the stretched optical pulses. Then an arbitrary waveform generator (AWG) (Tektronix AWG70000A) synchronized to the MLL is used to generate sinusoidal signals whose frequencies and initial phases are designed as described above. A 12.5-Gb/s Mach-Zehnder modulator (MZM) (PHOTLINE MX-LN-10) is driven by the generated sinusoidal signals for spectral encoding of the input optical pulses. Then an optical circulator directs the spectrally encoded pulses into a diffraction grating with a groove density of 1200 lines per millimeter. Due to the angular dispersion of the diffraction grating, a 1-D rainbow beam is generated via wavelength-to-space mapping. Fig. 4 depicts the detailed structure of the rainbow beam, which presents different spatial frequencies (f and $2f$) and initial phases (0, $\pi/2$, π and $3\pi/2$). The figures on the left give the intensity distribution curve of the 1-D rainbow beam and the figures on the right are the corresponding spatial patterns, exhibiting sinusoidal intensity distributions. The resultant 1-D rainbow beam passes through an objective lens with a focal length of 10 mm (Mitutoyo, 20$\times$, M Plan Apo NIR, NA 0.40) and focused on the flowing cells in a microfluidic channel. The flow direction is normal to the scan direction for 2-D image acquisition. The reflected optical pulses carrying the spatial information of the cells re-enter the diffraction grating followed by the circulator. A section of single mode fiber (SMF) with a length of 80 km and a complementary GVD of 17 ps/nm/km is used to perform pulse compression. The energy of the compressed pulses is finally detected by a 1.2-GHz photodiode (THORLABS DET01CFC/M) and sampled by an externally-clocked analog-to-digital converter (ADC) synchronized to the MLL. Image reconstruction can be performed by only applying IDFT to the captured measurements.

In the experiment, the microfluidic device is a necessity where the cells are controlled to flow at a uniform velocity, focused and ordered in the microfluidic channel by intrinsic inertial lift forces. Herein, the device is fabricated in thermoset polyester to ensure the rigidity of the microfluidic channel. It is important because the undesirable fluid dynamics and optical effects will be caused if the channel deforms. The dimensions of the microfluidic device used in the experiment are 120 μm width, 60 μm height and 2.2 cm length. The cells in the channel are controlled to flow at a speed of 1 m/s and the throughput is calculated from the volume rate and cell concentration to be approximately 30,000 cells/s. The specifications of the microfluidic device are described as Table 1.

There are two important parameters that are used to evaluate the performance of our prototype system: the compression ratio R and the frame rate F.

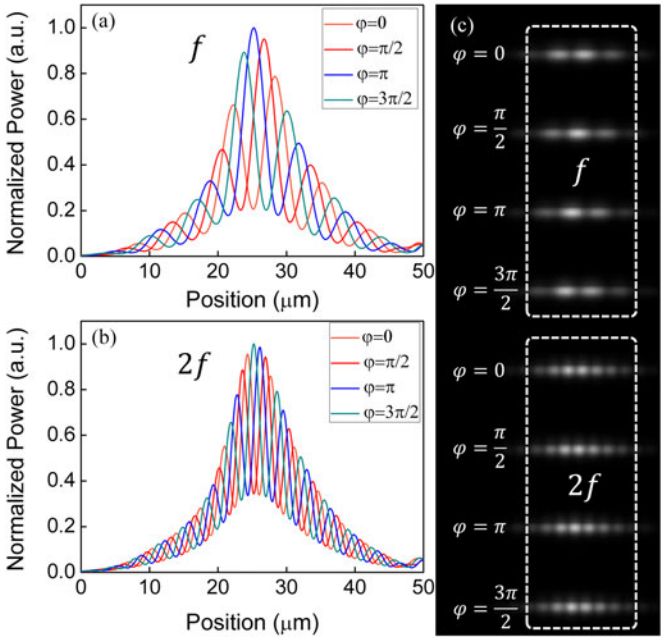

Fig. 4. Intensity fluctuations of the encoding scan lines with a spatial frequency of (a) f and (b) $2f$ and four phases (0, $\pi/2$, π and $3\pi/2$). The horizontal axis denotes different spatial positions on the scan line, and the vertical axis is the normalized power. (c) Corresponding spatial patterns of the scan lines, exhibiting sinusoidal intensity distributions.

TABLE 1
Specifications of the Microfluidic Device

Parameter	Value
Dimensions of the microfluidic device	120 μm (width) 60 μm (height) 2.2 cm (length)
Volumetric flow rate (corresponding mean channel velocity)	0.576 mL/min (1m/s)
Channel material	Polydimethylsiloxane (PDMS)
Maximum pressure	≥ 25 psi
Light transmittance	92%

In general, most information of a natural image concentrates on low-frequency components. If we acquire the Fourier spectrum of the image in the order from low to high frequencies, the quality of the reconstructed image is improved with a rapid convergence speed. This approach enables our system to perform lossy image compression. The compression ratio R is used to measure the capability of compressing volume data and is expressed as

$$R = \frac{M}{N} \tag{7}$$

where M is the number of measurements acquired for image reconstruction. N is the total number of pixels that 1-D illuminated scene contains, which is determined by the spectral bandwidth of the

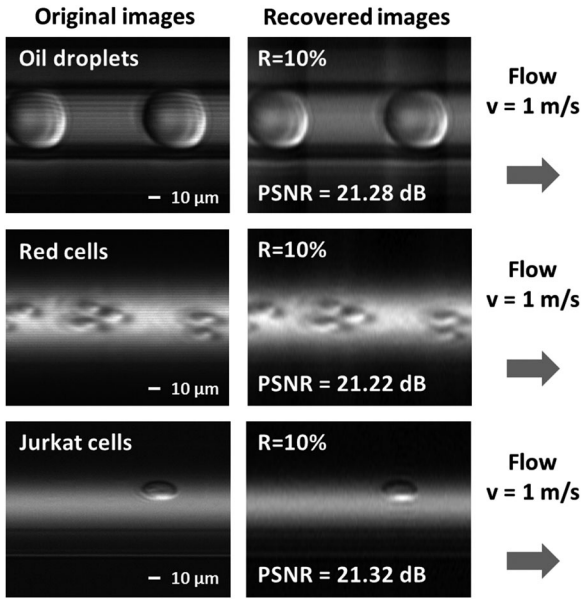

Fig. 5. Original (on the left) and reconstructed (on the right) snapshots of particles (including oil emulsion, red cells, and Jurkat cells) flowing at 1 m/s in the microfluidic channel. The compression ratio is 10%, and the PSNRs of the reconstructed images are also given.

optical pulse $\Delta\lambda$, the GVD of the DCF D and the sampling rate of the digitizer f_s [15]. To evaluate the quality of the reconstructed image, the original scene directly acquired from the time-stretch microscope [16] should also be obtained. Therefore, in our experiment, the generated illumination patterns are composed of sinusoidal patterns and uniform patterns. An additional digital storage oscilloscope (DSO) (Agilent Infiniium DSO91204A) with a sampling rate of 40 GS/s and a bandwidth of 13 GHz is used to acquire the data stream before pulse compression. Herein, $N = \Delta\lambda \cdot |D| \cdot f_s$, where $\Delta\lambda$ is 15 nm, D is -1368 ps/nm, and f_s is 40 GS/s. By substituting these parameters, N is calculated to be 800.

On the other hand, the frame rate of our prototype system is referred to as

$$F = \frac{f_{rep}}{M} \tag{8}$$

where f_{rep} is the pulse repetition rate (50 MHz). From (7) and (8), it can be seen that the frame rate of our system is inversely proportional to the number of measurements M, whereas the compression ratio R is proportional to the number of measurements M. Therefore, a trade-off between the frame rate and the compression ratio should be taken into consideration.

4. Experimental Results

To demonstrate the feasibility of our scheme, we implement an imaging flow cytometer for high-throughput screening. In the experiment, various biological samples including oil droplets, red cells and Jurkat cells are tested by our imaging system. Fig. 5 shows the original and reconstructed snapshots of the flowing particles in the microfluidic channel. Here the particles are controlled to flow at a uniform speed of 1 m/s and the throughput is calculated to be approximately 30,000 cells/s. The figures on the left present the original images directly captured by the DSO and the figures on the right are the corresponding reconstructed images at a compression ratio of 10% (80 measurements). The peak signal-to-noise ratios (PSNRs) of the reconstructed images are 21.28 dB, 21.22 dB, and 21.32 dB, respectively, implying a reliable reconstruction. In addition, the

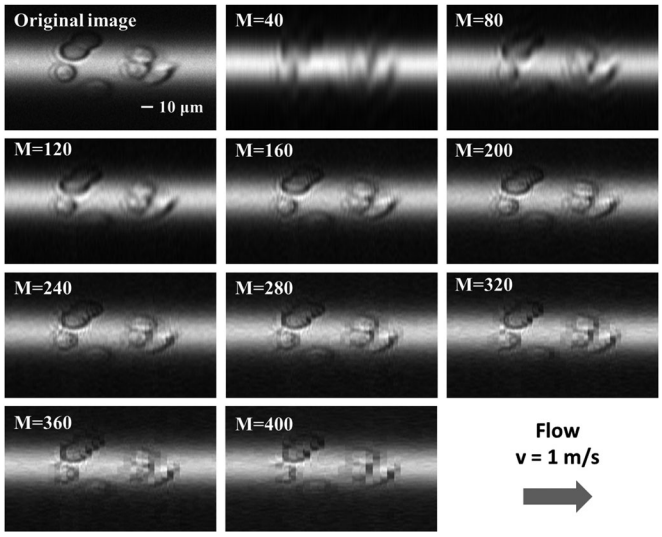

Fig. 6. Reconstructed images with different number of measurements. The flow speed is 1 m/s.

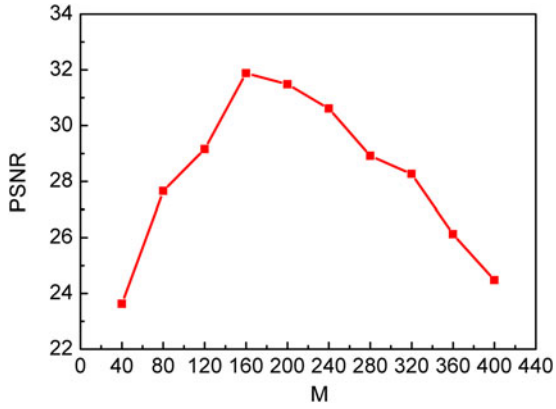

Fig. 7. PSNR as a function of increasing number of measurements.

frame rate of the imaging flow cytometer is 625 kHz, which is sufficiently high for screening of flowing particles.

Here, we analyze the effect of the imaging frame rate on reconstruction accuracy. Since the flow speed (1 m/s) is very slow relative to the scan rate (50 MHz), the image changes very slowly across a group of scanlines. If the flow speed is fixed, the number of measurements assigned to a frame is governed by the imaging frame rate. Fig. 6 presents the reconstructed snapshots with different number of measurements. Fig. 7 gives the PSNR curve corresponding to the reconstruction results in Fig. 6. From Fig. 7, we can see that the PSNR as a function of increasing number of measurements first increases, reaches a maximum, and then decreases. Too few measurements leads to information loss and too many measurements makes it difficult to keep the image nearly unchanged over a long acquisition period, both of which will degrade the quality of the reconstructed images. Therefore, the number of measurements used for image reconstruction should be designed carefully, for the purpose of achieving accurate reconstruction and high frame rates simultaneously.

Further, as the image acquisition is performed in the frequency domain, we also investigate the acquired Fourier spectrum at different compression ratios. Fig. 8 gives the reconstruction results of a certain 1-D image from Fig. 6. The Fourier spectrum of this original 1-D image (black line) and

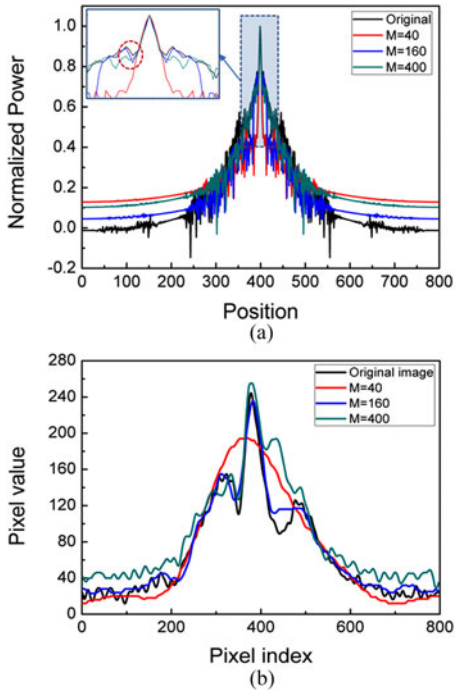

Fig. 8. Acquired Fourier spectrum and the corresponding reconstructed images. (a) The Fourier spectrum of the original 1-D image (black line) and the Fourier spectrum of the reconstructed images using 40 measurements (red line), 160 measurements (blue line), and 400 measurements (green line). (Inset) Zoom-in view of the low-frequency spectrum. (b) Profiles of the corresponding reconstructed 1-D images.

the Fourier spectrum of the reconstructed images using 40 measurements (red line), 160 measurements (blue line), and 400 measurements (green line) are presented in Fig. 8(a). An inset in Fig. 8(a) gives a zoom-in view of the low frequency spectrum, indicating that the Fourier spectrum of the reconstructed image using 160 measurements is most similar to the original spectrum. Fig. 8(b) presents the profiles of the reconstructed 1-D images using different number of measurements, also showing that the image reconstructed from 160 measurements has the highest accuracy.

In such an image compression system, only the Fourier coefficients of the low spatial frequency components are acquired, which means that some image details (containing the high spatial frequency information) may be lost during the reconstruction process. Therefore the resolution of the reconstructed image is governed by the number of measurements. It can be improved if more measurements are captured. However, when imaging a dynamic scene (e.g., screening of flowing cells), acquiring too many measurements may also lead to degradation of reconstruction accuracy as shown in Fig. 7. Therefore, the number of measurements required for image reconstruction needs to be carefully considered to achieve a trade-off between resolution and accuracy.

Compared with the CS-based SPI scheme, the primary advantage of our scheme is its capability of performing real-time image reconstruction. To demonstrate this property, we compare the computational time of image reconstruction in our scheme with that in CS-based SPI scheme. In both schemes, the number of measurements and the number of pixels are set to 80 (M) and 800 (N), respectively. Different reconstruction algorithms, two-step iterative shrinkage/thresholding algorithm (TWIST), gradient projection for sparse reconstruction (GPSR) for the CS-based SPI scheme and IFFT for our scheme, are used to perform image reconstruction and their computational time is also calculated. The TWIST and the GPSR are both iterative optimization algorithms. According to [27]–[31], the computational complexity of each iteration of TWIST and GPSR is O(N log(N)) and

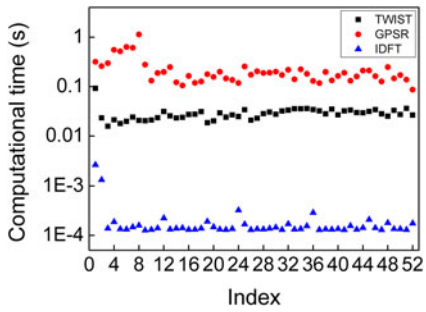

Fig. 9. Comparison of the reconstruction time between the CS-based SPI scheme and our proposed scheme. The TWIST algorithm and GPSR algorithm are used in the CS-based SPI scheme, and the IFFT is used in our scheme. Herein, 52 reconstructions are performed for each reconstruction algorithm.

$O(M \cdot N)$, respectively. In addition, in terms of TWIST and GPSR, accurately predicting the number of iterations for finding an approximate solution is impossible [30], [31]. However the number of iterations is related to the scale of the sensing matrix and the specified error threshold. To achieve a threshold of 10^{-4} (common in image reconstruction), lots of iterations are needed. In our scheme, no iterative algorithm is performed and only an IFFT operation is required. The computational complexity of IFFT is $O(M \log(M))$. Therefore, the computational complexity involved in our scheme is several orders of magnitude lower than that in the CS-based SPI scheme. Next we experimentally demonstrate the aforementioned analysis. On condition that the reconstruction error is fixed, the computational time of different algorithms is calculated. The experiment is repeated 52 times. The results in Fig. 9 show that the computational time of the GPSR algorithm is around 0.3 s, and if we use the TWIST algorithm, the time is reduced to about 0.03 s. In our scheme, the computational time of IFFT is two orders of magnitude lower, approximately 2×10^{-4} s. All these operations are performed using MATLAB (Intel Core i3-3220 CPU @ 3.30 GHz, 4.00 GB RAM). The reconstruction will be further accelerated if high-speed DSPs are used. Therefore, our scheme provides a promising solution to real-time imaging of flowing cells.

5. Conclusion

In summary, we demonstrate high-speed compressive microscopy of flowing cells using sinusoidal illumination patterns for Fourier spectrum acquisition. An imaging flow cytometer for high-throughput screening is implemented, achieving a frame rate of 625 kHz and a throughput of 30 000 cells/s. Simultaneously, the imaging flow cytometer also achieves real-time image reconstruction that is impossible to implement using the previous CS-based SPI scheme. Our scheme not only offers the capability of observing dynamic phenomena, but also relieves pressure on data transmission, processing and storage in real-time imaging, which can be widely applied in industrial quality control and label-free biomedical imaging.

References

[1] M. Levoy, "Light fields and computational imaging," *IEEE Computer*, vol. 39, no. 8, pp. 46–55, Aug. 2006.
[2] B. Sun *et al.*, "3D computational imaging with single-pixel detectors," *Science*, vol. 340, no. 6134, pp. 844–847, May 2013.
[3] J. Hunt *et al.*, "Metamaterial apertures for computational imaging," *Science*, vol. 339, no. 6117, pp. 310–313, Jan. 2013.
[4] D. L. Donoho, "Compressed sensing," *IEEE Trans. Inf. Theory*, vol. 52, no. 4, pp. 1289–1306, Apr. 2006.
[5] E. J. Candès, J. Romberg, and T. Tao, "Robust uncertainty principles: Exact signal reconstruction from highly incomplete frequency information," *IEEE Trans. Inf. Theory*, vol. 52, no. 2, pp. 489–509, Jan. 2006.
[6] M. F. Duarte *et al.*, "Single-pixel imaging via compressive sampling," *IEEE Signal Process. Mag.*, vol. 25, no. 2, pp. 83–91, Mar. 2008.

[7] W. L. Chan, K. Charan, D. Takhar, K. F. Kelly, R. G. Baraniuk, and D. M. Mittleman, "A single-pixel terahertz imaging system based on compressed sensing," *Appl. Phys. Lett.*, vol. 93, no. 12, Sep. 2008, Art. no. 121105.
[8] F. Magalhães, F. M. Araújo, M. V. Correia, M. Abolbashari, and F. Farahi, "Active illumination single-pixel camera based on compressive sensing," *Appl. Opt.*, vol. 50, no. 4, pp. 405–414, Jan. 2011.
[9] S. S. Welsh, M. P. Edgar, R. Bowman, P. Jonathan, B. Sun, and M. J. Padgett, "Fast full-color computational imaging with single-pixel detectors," *Opt. Exp.*, vol. 21, no. 20, pp. 23068–23074, Sep. 2013.
[10] Z. Zhang, X. Ma, and J. Zhong, "Single-pixel imaging by means of Fourier spectrum acquisition," *Nature Commun.*, vol. 6, Feb. 2015, Art. no. 6225.
[11] M. P. Edgar *et al.*, "Simultaneous real-time visible and infrared video with single-pixel detectors," *Sci. Rep.*, vol. 5, May 2015, Art. no. 10669.
[12] L. Bian *et al.*, "Multispectral imaging using a single bucket detector," *Sci. Rep.*, vol. 6, Apr. 2016, Art. no. 24752.
[13] F. Soldevila, P. Clemente, E. Tajahuerce, N. Uribe-Patarroyo, P. Andrés, and J. Lancis, "Computational imaging with a balanced detector," *Sci. Rep.*, vol. 6, Jun. 2016, Art. no. 29181.
[14] K. Goda, K. K. Tsia, and B. Jalali, "Serial time-encoded amplified imaging for real-time observation of fast dynamic phenomena," *Nature*, vol. 458, no. 7242, pp. 1145–1149, Apr. 2009.
[15] K. K. Tsia, K. Goda, D. Capewell, and B. Jalali, "Performance of serial time-encoded amplified microscope," *Opt. Exp.*, vol. 18, no. 10, pp. 10016–10028, Apr. 2010.
[16] K. Goda *et al.*, "High-throughput single-microparticle imaging flow analyzer," *Proc. Nat. Acad. Sci. USA*, vol. 109, no. 29, pp. 11630–11635, Jul. 2012.
[17] A. C. Chan, A. K. Lau, K. K. Wong, E. Y. Lam, and K. K. Tsia, "Arbitrary two-dimensional spectrally encoded pattern generation—a new strategy for high-speed patterned illumination imaging," *Optica*, vol. 2, no. 12, pp. 1037–1044, Dec. 2015.
[18] C. Lei, B. Guo, Z. Cheng, and K. Goda, "Optical time-stretch imaging: Principles and applications," *Appl. Phys. Rev.*, vol. 3, no. 1, Feb. 2016, Art. no. 011102.
[19] H. Chen *et al.*, "High speed single-pixel imaging via time domain compressive sampling," in *Proc. Conf. Lasers ElectroOpt.*, Jun. 2014, paper JTh2A.132.
[20] B. T. Bosworth and M. A. Foster, "High-speed flow imaging utilizing spectral-encoding of ultrafast pulses and compressed sensing," in *Proc. Conf. Lasers ElectroOpt.*, Jun. 2014, paper ATh4P.3.
[21] B. T. Bosworth, J. R. Stroud, D. N. Tran, T. D. Tran, S. Chin, and M. A. Foster, "High-speed flow microscopy using compressed sensing with ultrafast laser pulses," *Opt. Exp.*, vol. 23, no. 8, pp. 10521–10532, Apr. 2015.
[22] Q. Guo, H. Chen, Z. Weng, M. Chen, S. Yang, and S. Xie, "Fast time-lens-based line-scan single-pixel camera with multi-wavelength source," *Biomed. Opt. Exp.*, vol. 6, no. 9, pp. 3610–3617, Aug. 2015.
[23] X. Su and W. Chen, "Fourier transform profilometry: A review," *Opt. Lasers Eng.*, vol. 35, no. 5, pp. 263–284, Feb. 2001.
[24] M. H. Asghari and B. Jalali, "Discrete anamorphic transform for image compression," *IEEE Signal Process. Lett.*, vol. 21, no. 7, pp. 829–833, Jul. 2014.
[25] M. H. Asghari and B. Jalali, "Experimental demonstration of optical real-time data compression," *Appl. Phys. Lett.*, vol. 104, no. 11, Mar. 2014, Art. no. 111101.
[26] C. L. Chen, A. Mahjoubfar, and B. Jalali, "Optical data compression in time stretch imaging," *PLoS One*, vol. 10, no. 4, Apr. 2015, Art. no. e0125106.
[27] T. Blumensath and M. E. Davies, "Iterative hard thresholding for compressed sensing," *Appl. Comput. Harmon. Anal.*, vol. 27, no. 3, pp. 265–274, May 2009.
[28] J. A. Tropp and A. C. Gilbert, "Signal recovery from random measurements via orthogonal matching pursuit," *IEEE Trans. Inf. Theory*, vol. 53, no. 12, pp. 4655–4666, Dec. 2007.
[29] D. Needell and J. A. Tropp, "CoSaMP: Iterative signal recovery from incomplete and inaccurate samples," *Appl. Comput. Harmon. Anal.*, vol. 26, no. 3, pp. 301–321, Jan. 2009.
[30] J. M. Bioucas-Dias and M. A. Figueiredo, "A new TwIST: two-step iterative shrinkage/thresholding algorithms for image restoration," *IEEE Trans. Image Process.*, vol. 16, no. 2, pp. 2992–3004, Nov. 2007.
[31] M. A. Figueiredo, R. D. Nowak, and S. J. Wright, "Gradient projection for sparse reconstruction: Application to compressed sensing and other inverse problems," *IEEE J. Sel. Topics Signal Process.*, vol. 1, no. 4, pp. 586–597, Jan. 2008.